Understanding activity and selectivity of metal-nitrogen-doped carbon catalysts for electrochemical reduction of CO$_2$

Wen Ju[1], Alexander Bagger[2], Guang-Ping Hao [3], Ana Sofia Varela[1,4], Ilya Sinev[5], Volodymyr Bon [3], Beatriz Roldan Cuenya[5,6], Stefan Kaskel[3], Jan Rossmeisl[2] & Peter Strasser[1]

Direct electrochemical reduction of CO$_2$ to fuels and chemicals using renewable electricity has attracted significant attention partly due to the fundamental challenges related to reactivity and selectivity, and partly due to its importance for industrial CO$_2$-consuming gas diffusion cathodes. Here, we present advances in the understanding of trends in the CO$_2$ to CO electrocatalysis of metal- and nitrogen-doped porous carbons containing catalytically active M–N$_x$ moieties (M = Mn, Fe, Co, Ni, Cu). We investigate their intrinsic catalytic reactivity, CO turnover frequencies, CO faradaic efficiencies and demonstrate that Fe–N–C and especially Ni–N–C catalysts rival Au- and Ag-based catalysts. We model the catalytically active M–N$_x$ moieties using density functional theory and correlate the theoretical binding energies with the experiments to give reactivity-selectivity descriptors. This gives an atomic-scale mechanistic understanding of potential-dependent CO and hydrocarbon selectivity from the M–N$_x$ moieties and it provides predictive guidelines for the rational design of selective carbon-based CO$_2$ reduction catalysts.

[1] Department of Chemistry, Chemical Engineering Division, Technical University Berlin, Berlin 10623, Germany. [2] Department of Chemistry, University of Copenhagen, Universitetsparken 5, Copenhagen 2100, Denmark. [3] Department of Inorganic Chemistry, Technical University Dresden, Dresden 01062, Germany. [4] Institute of Chemistry, National Autonomous University of Mexico, Mexico City 04510, Mexico. [5] Department of Physics, Ruhr University Bochum, Bochum 44801, Germany. [6] Interface Science Department, Fritz-Haber-Institut der Max-Planck Gesellschaft, 14195 Berlin, Germany. Wen Ju and Alexander Bagger contributed equally to this work. Correspondence and requests for materials should be addressed to G.-P.H. (email: guangping.hao@manchester.ac.uk) or to J.R. (email: jan.rossmeisl@chem.ku.dk) or to P.S. (email: pstrasser@tu-berlin.de)

irect electrochemical reduction of CO_2 (CO_2RR) is a promising early-stage technology to produce commodity chemicals and synthetic fuels. Electricity from renewable sources can provide the input power needed to react water and waste CO_2 to produce carbon-based chemicals or fuels in a sustainable manner[1]. The ultimate technological viability of this process, however, is contingent upon the identification of affordable catalyst materials that overcome the challenges regarding the poor product selectivity and poor voltage and energy efficiency[2].

Metals have been the most common choice as electrocatalysts for the CO_2RR. In early studies, copper was found to be the unique metal able to reduce CO_2 into relevant amounts of hydrocarbons[3]. This is why catalysis studies—whenever hydrocarbon products were of primary interest—have invariably focused on Cu or Cu-derived materials. From these we now know that the reaction conditions such as electrolyte[4–6] and applied potential[3, 7] can have a significant effect on activity and selectivity of Cu during the catalytic reaction process. In addition, more recent work evidenced that the morphology of the copper electrode[8], its oxidation state[9, 10], the geometric shape[11–14] and size[15] of the Cu nanoparticles, the interparticle distance[16, 17], as well as the presence of a second metal[18–20] also play a crucial role for the resulting catalytic performance.

In contrast to hydrocarbon formation, the CO_2 reduction to CO requires only two electron/proton transfers, which makes it a substantially less hindered process. The formation of CO is usually accompanied by HER resulting in syngas production, which can be used as feedstock in synthetic fuels production via the catalytic Fischer-Tropsch process. The chloralkaline electrolysis-based polyurethane and polycarbonate industries, however, strive to adopt an electrocatalytic cathodic reduction of CO_2 to pure CO streams for production of phosgene intermediate further downstream. Such innovative CO_2-depletion cathodes coupled to the anodic chlorine production electrode are still in early-stage research and currently require first and foremost fundamental advances in our understanding of the catalytic mechanism and the identification of suitable efficient catalysts.

It has been shown that Ag[21, 22], Au-derived[23–28] and bimetallic Cu–In[19] and Cu–Sn[20] catalysts can selectively reduce CO_2 to CO at low overpotentials. However, despite their promising performance, alternative earth-abundant catalyst materials are desired. Molecular catalysts based on Iron-Porphyrin showed some CO_2 to CO reactivity in DMF solution[29–31], and so did metal-organic frameworks[32] and immobilized porphyrins[33–35]. Unfortunately, these material concepts severely suffer from low electric conductivity and hence are not suitable as CO_2 reduction catalysts at large current densities.

A promising recent alternative to expensive noble metals are solid doped carbon-based powder catalysts, similar to those developed for oxygen reduction reaction in recent years[36–40]. In recent studies, metal-free, nitrogen-doped carbon catalysts (N–C) have been proven capable to efficiently reduce CO_2 to single- and multi-carbon species and both experimental and computational studies have pointed toward pyridinic-N as the active site[41–46]. More recent studies evidenced that the metal centers are in fact crucial for the CO_2RR to CO. Varela et al.[33] have tested the PANI-derived catalysts as CO_2RR catalyst and shown that the addition of metal resulted in a strongly enhanced CO_2RR activity and the generation of CO. More interestingly, trace amounts of CH_4 were detected[33]. Consistently, DFT studies on transition metal based porphyrin-like catalysts suggested that depending on the metal center, *CO can be further reduced[47, 48]. A detailed fundamental mechanistic understanding of the CO_2 reduction reactivity and selectivity of single-site metal-nitrogen-doped carbons is still missing. This contribution will change that.

Here, we explore an entire family of single site, N-coordinated transition metal-doped nanoporous carbon materials (henceforth
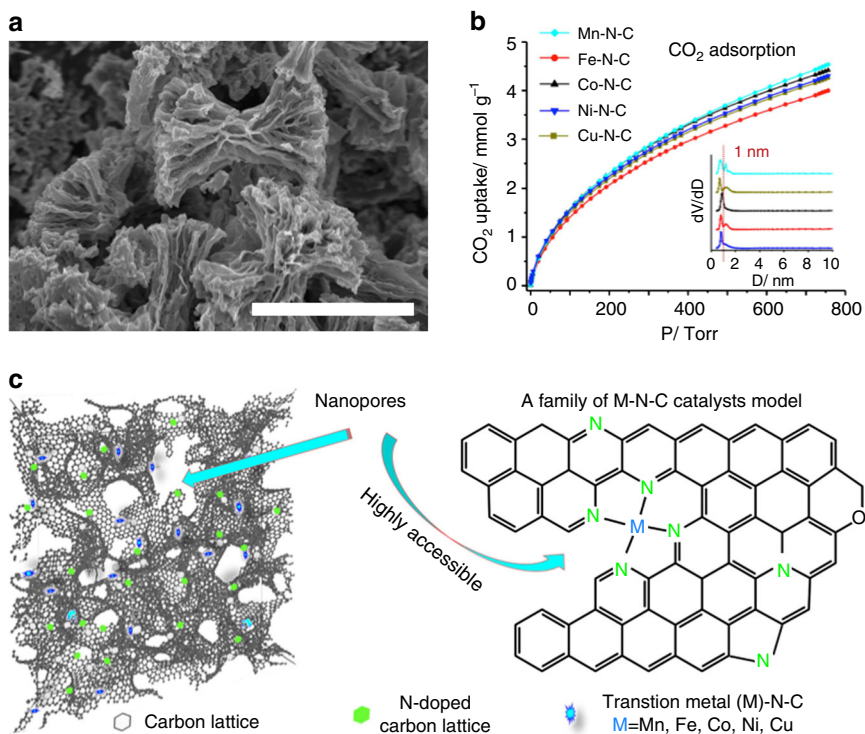
Fig. 1 Visualization, porosity and illustration of the M–N–C catalyst. **a** Typical SEM image of the family of N-coordinated metal-doped (M–N–C) carbon electro-catalysts, scale bar=4 µm; **b** CO_2 physisorption isotherm (273 K); inset: the pore size distribution; **c** Materials model and a schematic local structure
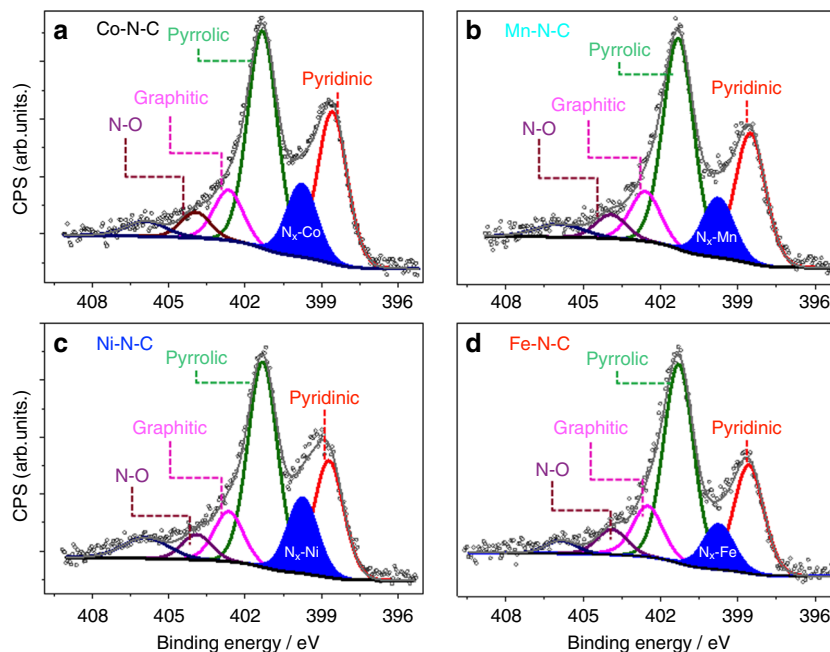
Fig. 2 High-resolution XPS characterization. N-1s XPS core level region of **a** Co, **b** Mn, **c** Ni and **d** Fe doped M–N–C catalyst. The $2p_{3/2}$ spectra of the corresponding metal peaks (Co-2p, Mn-2p, Ni-2p, Fe-2p) is shown in Supplementary Fig. 9

referred to as M–N–C catalysts) as single-site electro-catalysts for the CO_2RR. Using a combined experimental and computational approach we investigate the catalyst activity and product efficiency (catalyst selectivity) and unravel their mechanistic origins in terms of binding energies and energetic reaction paths. This family of M–N–C materials comprises highly accessible and homogeneously dispersed $M–N_x$ sites, displays balanced surface wettability and low valence metal species, which exhibit impressively high activity and remarkable selectivity at low overpotential for the CO_2RR to CO and hydrocarbons. We show that these catalysts are comparable alternatives to Au-based catalysts in future industrial CO_2-consumption gas diffusion cathodes (CCCs). Density functional theory (DFT) calculations offer first-of-its-kind mechanistic insight into the rate- and selectivity determining processes on the single-site metal-nitrogen centers. We show that the binding energies of intermediates to the $M–N_x$ moieties provide excellent descriptors to predict, and understand the mechanistic details of the CO_2RR activity and selectivity of this family of catalysts over a wide overpotential range.

Results

Synthesis and characterization. We have synthesized a family of M–N–C electrocatalysts starting with bipyridine-based coordinated polymers and a variety of transition metals such as Mn, Fe, Co, Ni, and Cu. Materials characterization started with morphological and gas adsorption experiments (Fig. 1a, b). The M–N–C electrocatalysts showed hierarchical chemical structures with visible macropores (Fig. 1a, Supplementary Fig. 1). The pore size distribution peaks narrowly at ca. 0.7–0.8 nm (2.5–2.9 times of the dynamic diameter of CO_2 molecules, Fig. 1b inset), enabling this family M–N–C materials a remarkable 4.0–4.5 mmol g^{-1} capacity for CO_2 capture at atmospheric pressure (Fig. 1b) due to their high-adsorption potential to trap CO_2 molecules[49]. This could result in CO_2 enrichment within a local environment despite the low CO_2 solubility in the working electrolyte. Figure 1c displays a structural illustration of the interconnected macropore walls, composed of thin carbon branches with highly accessible micropores, all over which the

coordinated metal sites as well as N-containing carbon lattice are homogeneously distributed.

The N_2 physisorption isotherms (Supplementary Fig. 2) are essentially type I for Cu, Co, Ni, or Mn–N–C samples, indicating their microporous nature, while the visible hysteresis of Fe–N–C material reveals the presence of a small fraction of mesopores in addition to micropores. Notably, a significant increase of gas uptake was observed at higher relative pressure ($P/P_0 > 0.9$) for all M–N–C samples, indicating their rich macroporosity, which is consistent with the SEM images (Fig. 1a). The specific surface area based on Brunauer–Emmett–Teller (BET) theory is in range of 615–938 $m^2 g^{-1}$, while the Ni–N–C and Mn–N–C show the lowest and the highest BET surface area, respectively, and the others are in between (Supplementary Table 1). This shows a roughly linear relationship with the double layer capacity under the electrochemical condition (Supplementary Fig. 3, Supplementary Table 1). The M–N–C samples showed a moderate hydrophilic character (Supplementary Fig. 4) and comparable defect site density (Supplementary Fig. 5, Supplementary Table 2). The XRD patterns (Supplementary Fig. 6) reflect the predominant amorphous carbon support, particularly for Mn, Co, Ni or Cu–N–C; while the presence of Fe, to some extent, led to graphitic domains. Some residual Fe, Co, Ni in a metallic state was detectable after the H_2 reduction at 900 °C. The STEM elemental mappings (Supplementary Fig. 7) are fully consistent with the XRD findings showing presumably carbon-encapsulated metal particles as well as coordinated metal ion sites for the three catalysts.

Catalyst surface. The catalyst surface chemical composition and state were investigated using X-ray photoelectron spectroscopy (XPS). Fitted high-resolution N 1 s spectra (Fig. 2 for Co, Mn, Ni, Fe, and Supplementary Fig. 8 for Cu, detailed fitted parameters in Supplementary Table 3) evidenced the presence of the porphyrin-like metal-coordinated $M–N_x$ moieties (399.7 eV), as well as pyrrolic (401.3 eV), pyridinic (398.6 eV), graphitic (402.5 eV), and $N–O_x$ (403.9 eV) species (Fig. 2)[50, 51]. In addition, a weak and broad peak can be fitted at higher binding energies, centered at 405.9 eV, which is likely assigned to trace amounts of
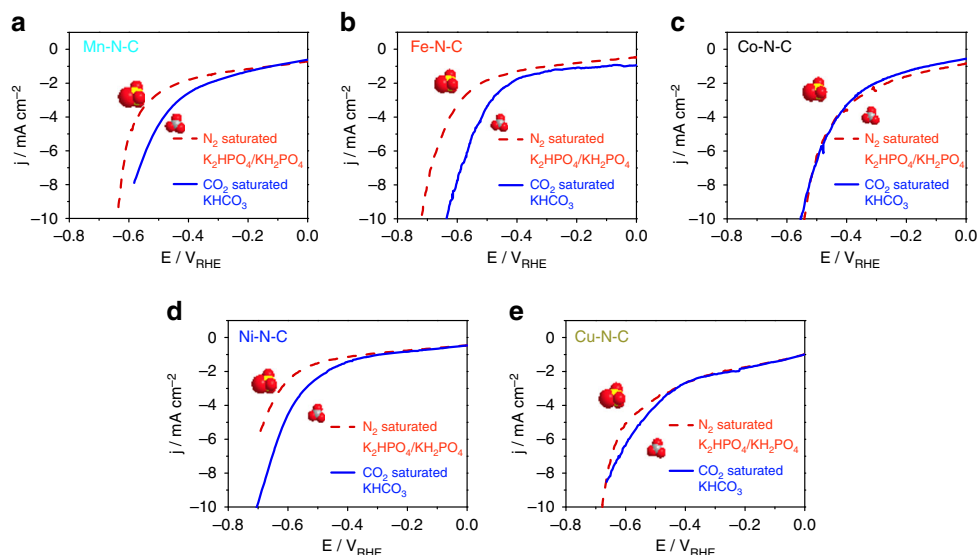
Fig. 3 CO_2 reduction reaction activities. Linear sweep voltammetry of **a** Mn–N–C, **b** Fe–N–C, **c** Co–N–C, **d** Ni–N–C and **e** Cu–N–C in CO_2-saturated 0.1 M $KHCO_3$ (solid lines) and in N_2-saturated 0.1 M KH_2PO_4/K_2HPO_4 (dashed lines) with a catalyst loading of 0.76 mg cm^{-2} at 5 mV s^{-1} in cathodic direction
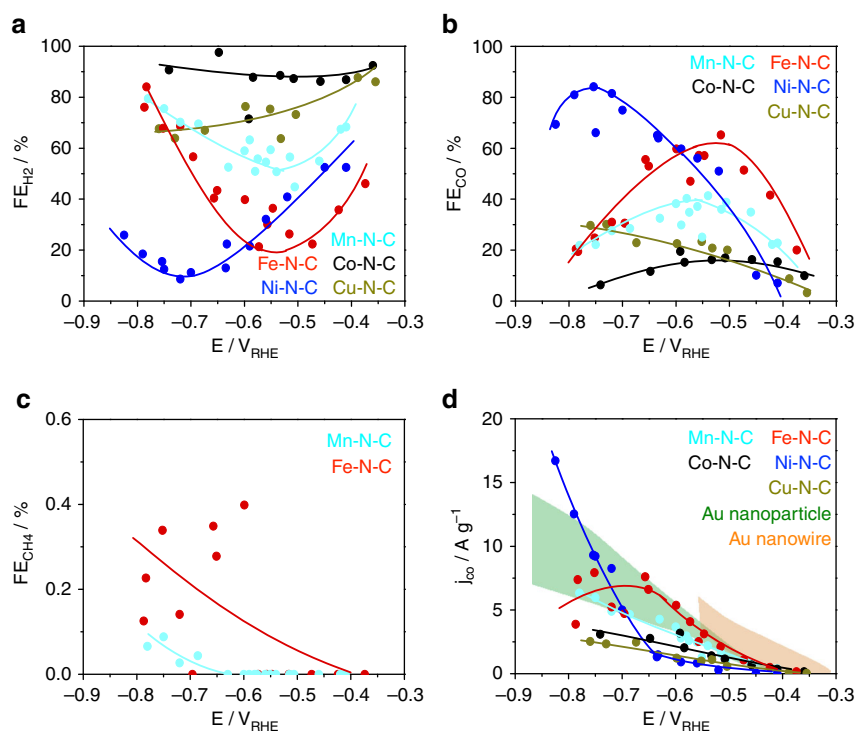

Fig. 4 Catalytic performance and product analysis. **a–c** Faradaic Efficiencies (FE) vs. applied, IR-corrected electrode potential of **a** H_2, **b** CO and **c** CH_4. **d** Catalyst mass-normalized CO partial currents (mass activity) vs. applied potential for the five M–N–C catalysts compared to state-of-art Au catalysts (performance ranges of Au-nanoparticle and Au-nanowires are shown by filled areas[25–27]. Lines to guide the eye. Conditions: 60 min at constant electrode potential in CO_2-saturated 0.1 M $KHCO_3$ with 0.76 mg cm^{-2} M–N–C catalysts loading. Faradaic efficiencies and CO yields after 15 min are shown in Supplementary Fig. 11

non-decomposed nitrogen precursors[52]. The N 1 s spectra of all samples are dominated by pyrrolic nitrogen (Supplementary Table 3), whereas the M–N_x moiety gives rise to the most intense core level for the Ni-doped sample. A detailed analysis of the metal $2p_{3/2}$ shake-up photoemission lines (insets of Fig. 2) offering insight in the chemical state of the metallic species is presented in Supplementary Fig. 9. Combined, our materials characterization confirmed the prevalent presence of

N-coordinated metal single-site moieties, M–N_x, near the surface in all catalyst samples, except for the Cu sample that exhibited evidence of near-surface metallic Cu particles (Supplementary Fig. 8).

Catalytic sensitivity towards CO_2. As a first test of the total faradaic reactivity of our single-site solid catalysts in CO_2-saturated 0.1 M $KHCO_3$, comprising both the HER and CO2RR,
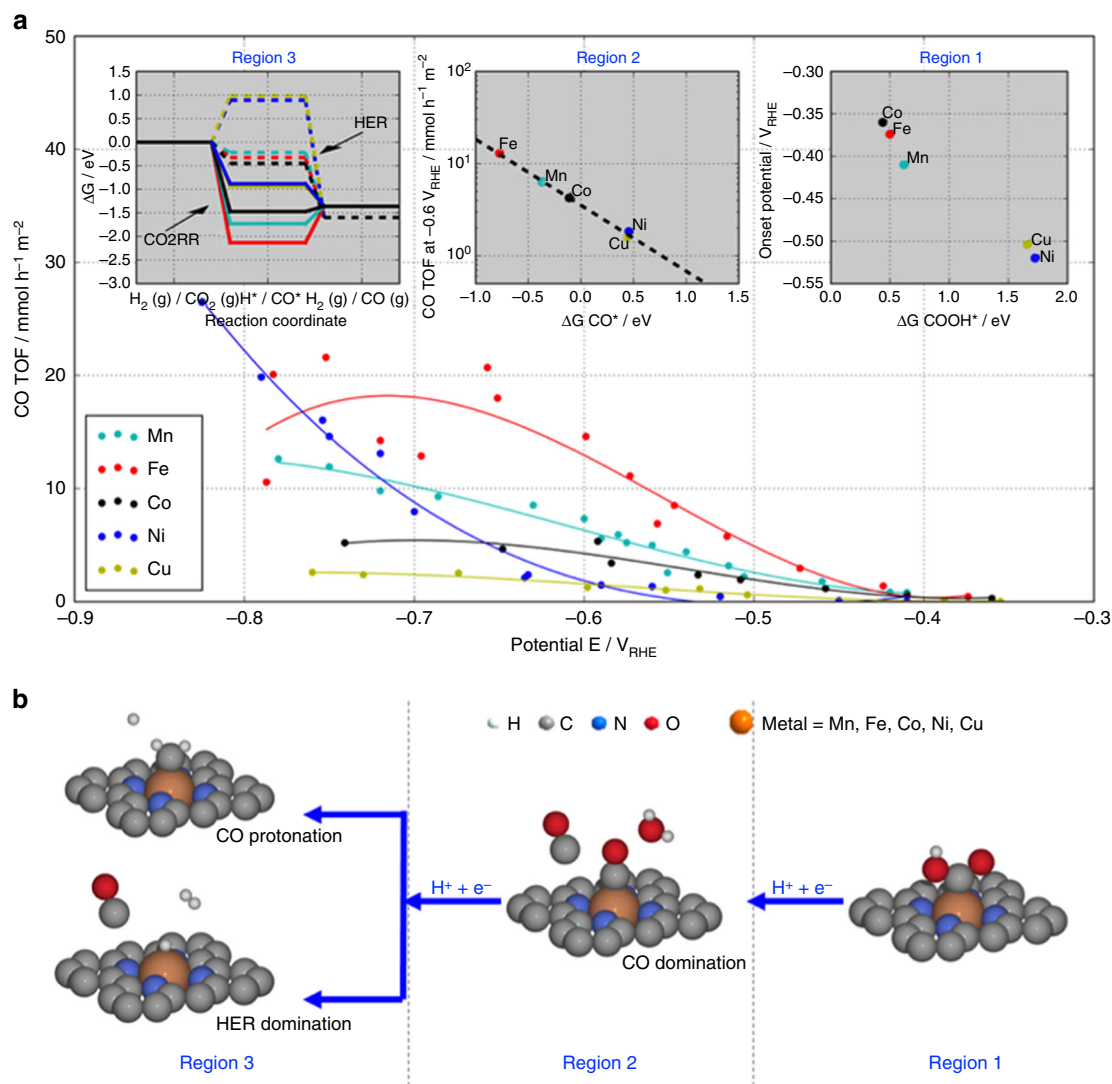
Fig. 5 Experimental correlation to simulations. Experimental CO production turnover frequency (TOF) of the M–N–C catalysts vs. applied IR-corrected electrode potential (see Supplementary Equation 4). The catalytic reactivity trends **a** and reaction pathway **b** split into 3 potential regions with distinctly different rate-determining mechanistic features. Insets: Region 1: Low overpotentials, the experimental onset potentials of CO production (better seen on the log (CO TOF)–E plot in Supplementary Fig. 15) correlate with the binding energy of the reaction intermediate COOH* taken from Supplementary Fig. 14. Region 2: Intermediate over-potentials, CO production TOF at -0.6 V_{RHE} correlates with the free energy of adsorbed CO, CO* taken from Supplementary Fig. 14; Region 3: High overpotentials, free energy diagrams for the HER (dashed paths) and CO2RR (solid paths) at -0.8 V_{RHE} for each M–N–C catalyst. HER barriers are high for Ni and Cu, while CO2RR is downhill making these materials favorable CO producing catalysts

Linear Sweep Voltammetry (LSV) were performed between 0.0 and -0.7 V vs. RHE, blue solid curves in Fig. 3. Comparison with LSVs performed in absence of CO_2 (red dashed curves) revealed substantial CO2RR activity of the Mn, Fe, Ni, and Cu-doped catalysts. Furthermore, the Mn, Fe, Ni, and Cu-doped samples exhibited an earlier onset (smaller overpotential) for the CO2RR than HER, suggesting that, at least in a small potential window, they are selective towards CO2RR. By contrast, Co–N–C presented a comparable activity suggesting that the HER may be the dominant faradic process over the investigated potential range.

Catalytic performance tests were conducted under potential control during 1 h electrolysis. The geometric electrode area-normalized (j_{geo}) and the active interfacial area-normalized (double-layer capacity-normalized) faradaic currents (j_{DL}) after 15 min and 60 min are compared in Supplementary Fig. 10. The Co–N–C catalyst generated the most overall faradaic current, while the Cu–N–C displayed the poorest overall reactivity at larger overpotentials, in accordance with Fig. 3.

Faradaic efficiencies and absolute yields. The stationary faradaic efficiencies (FE) of the three principal CO2RR products after 60 min electrolysis are displayed in Fig. 4. H_2 and CO accounts for up to 95% of the transferred charge on the single-site catalysts (see Supplementary Eqs. 1-3. Product distribution at 15 min is shown in Supplementary Fig. 11). Remarkably, small amounts of methane were detected, however only on Fe and Mn catalysts, while no liquid product could be detected. Despite the low number of active surface single-sites on the M–N–C catalysts, their mass-based CO partial currents (production rate) are comparable to that of Au-based catalysts[25, 26], especially at technologically interesting higher currents (Fig. 4d). These results highlight the significance of this family of compounds as non-precious, earth-abundant low-cost and efficient CO2RR catalyst alternatives for the electrochemical production of CO in CO_2-consuming electrodes.

To arrive at a fundamental mechanistic understanding of the CO_2 catalysis on the single-site materials, we focus on reactivity

trends among the M–N–C catalysts at different applied over-potentials. The CO_2RR performance tests exhibit a strong dependence on the nature of the transition metal, not only in terms of the molar CO/H_2 ratio, but also in the experimental overpotential at maximum CO efficiency (see Fig. 4a and b). H_2 FE on Co–N–C remains above 80% over the entire electrode potential range, making it a catalyst with poor selectivity towards CO_2RR. On the other hand, Fe–N–C and particularly Ni–N–C catalysts clearly act as highly promising catalyst for selective CO production, however, the maximum CO FE is obtained at a smaller overpotential on Fe–N–C ($V_{RHE} = -0.55$ V, $FE_{CO} = 65\%$) than on Ni-N-C ($V_{RHE} = -0.78$ V, $FE_{CO} = 85\%$). Note that the selectivity of these two single site catalysts is drastically different from that of metallic Ni and Fe catalysts, which yield H_2 as virtually the only major product[23]. We have conducted a number of control measurements to confirm that the $M–N_x$ site is indeed the most significant active center for CO_2 reduction into CO. First, the Nitrogen Free M–C as well as the polymer precursor before pyrolysis (Cu-Bpy) contributes negligibly to the CO activity during the CO_2RR process. Second, we could not exclude some catalytic activity of the Nitrogen functionalities. However, based on their finite CO_2RR catalytic reactivity and the rough similarity of the distribution in the M–N–C catalysts, their effect could be seen as a known weak background signal for all cases (Supplementary Table 3, Supplementary Fig. 12 and 13). This finding strongly suggests that the CO_2RR (to CO) reactivity trends purely originate from the differences in intrinsic catalytic activity of the various $M–N_x$ moieties.

Atomistic insight into the M–N–C activities. To bring theoretical mechanistic insight, DFT simulations pertaining to the CO_2 reduction process on N-coordinated metal-doped M–N–C catalysts were carried out. For this purpose we took the single-site motif $M–N_4$ as active site to calculate the binding energy of the different reaction intermediates (Supplementary Fig. 14). We note that there exist other $M–N_x$ functionalities[53–55]; however, previously we computationally found the metal to be the dominating factor as compared to other $M-N_x$ functionalities[56]. Thus, the $M–N_4$ site appears to be a reasonable single active site model for our analysis here. For the model we calculate the binding energies without electrolyte, which is reasonable for the trends and conclusions drawn here. While activity can often be associated with a single descriptor, selectivity can obviously not, as it is related to competition between different possible reaction paths. The different reaction paths show different dependence on metal center and potential.

Figure 5 compares the trends in the experimental CO-specific turnover frequencies (TOF) of the five M–N–C catalysts. The TOF values were derived from the absolute CO production rates normalized by the respective BET surface area-weighted surface $M–N_x$ concentration (Supplementary Equation 4). Correlating the experimental TOF trends and predicted DFT theoretical energy diagrams we were able to identify three regions of distinct reaction dynamics that control the electrocatalysis: First, Region 1, a dynamic regime at low overpotentials near the onset of the CO production, Then, Region 2, a dynamic regime at intermediate overpotentials and finally, Region 3, at larger overpotentials where the CO_2 reduction current densities approach technologically relevant levels. The reason for this division is that the order in catalytic activity change in the different regions indicating that the rate in the different regions is determined by a distinctly different surface chemistry.

Low overpotential regime around −0.45 V_{RHE} (Region 1). Defining the CO production onset potential to be the applied electrode potential at which the CO TOF exceeds 0.2 mmol/(h m^2_{active}), the Fe, Mn and Co–N–C catalysts start producing CO at around −0.4 V vs. RHE, while the Cu and Ni samples require considerable higher overpotentials, see Region 1 inset in Fig. 5. The onset potential is determined by the mechanistic elementary step that is the last to become exergonic as the overpotential is increased (limiting potential). Simulations suggest that this potential-determining step is the first proton-coupled electron transfer reduction of CO_2 to adsorbed COOH according to

$$CO_2 + H^+ + e^- \rightarrow COOH^* \qquad (1)$$

In agreement with electrochemical measurements, in the simulations the catalyst falls into two groups: Co, Fe and Mn requiring only a small overpotential, whereas Cu and Ni need a larger thermodynamic driving force for that step.

Intermediate overpotential regime around −0.6 V_{RHE} (Region 2). Here, the Fe- and Co–N–C catalysts approach their maximum CO_2RR reactivity, while the Ni–N–C catalyst has barely passed above its CO production onset. With the electrode potential being now past the limiting electrode potential, the overall CO_2 reduction reaction invariably becomes limited by a non-faradaic chemical reaction step. The larger the thermodynamic driving force of this step, the faster the overall reaction rate. Correlating experiments to DFT calculations reveals that the logarithm of the experimental CO TOF is now linearly related to the CO* binding energy descriptor, see Region 2 inset in Fig. 5. This suggests that the rate-controlling intermediate has shifted from COOH* to CO*. As a result of this, the overall reaction rate appears limited by the process

$$COOH^* + H^+ + e^- \rightarrow CO^* + H_2O \cdot \qquad (2)$$

While DFT predictions do not allow us to unambiguously pinpoint the exact rate-limiting point along the reaction coordinate of step (2), we hypothesize that it is the chemical dissociative formation of H_2O according to $COOHH^* \rightarrow CO^* + H_2O$. The stronger CO* binds, the more driving force is available for this step. An evidence for the hypothesis can be considered by comparing the Fe- and Mn–N–C, which have almost similar COOH* and H* binding. However, these descriptors cannot explain the experimental different CO TOF from the two, while the logarithm to the CO* descriptor can. (Supplementary Fig. 15)

Large overpotential regime <−0.7 V_{RHE} (Region 3). Here, the experimental CO formation TOF in Fig. 5, as well as the faradaic CO efficiencies of the Fe–N–C and Co–N–C catalysts have passed their maximum and trend downward (Fig. 4), that of Mn–N–C is levelling off, while the Ni–N–C catalyst continues to increase its CO production rate at a very high faradaic CO efficiency, significantly outperforming all other single-site catalysts as well as Au catalysts.

Our mechanistic DFT analysis shown in inset (Region 3) of Fig. 5 is able to consistently explain all these experimental findings. The free energy diagrams of the HER (dashed) and CO_2RR (solid) evidences that the Fe-, Co- and Mn-based catalysts start to strongly catalyze the hydrogen evolution reaction ($H^+ + e^- \rightarrow H^* \rightarrow H_{2(g)}$) illustrated by the all downhill reaction energy pathways. Among them, Co–N–C is the most efficient HER catalyst and, thus, displays the highest faradaic efficiency for hydrogen evolution, see Fig. 4. In contrast, the Ni- and Cu-based catalysts exhibit very weak binding of H* which makes the HER thermodynamically unfavorable at −0.8 V_{RHE}, giving rise to low faradaic hydrogen efficiencies.

The DFT predictions of the CO_2RR pathway ($CO_2 \rightarrow CO^* \rightarrow CO_{(g)}$) at −0.8 V_{RHE} complete the mechanistic picture. While the

Ni–N$_x$ and Cu–N$_x$ moieties stand out as the single sites with the weakest binding to COOH* and therefore with the largest overpotential to start CO$_2$ reduction (see Region 1), their weak binding of CO* prevents the potential-independent chemical CO-desorption process (CO* → CO$_{(g)}$) to become rate-limiting. This is in contrast with the Mn, Fe, Co–N$_x$ sites whose CO TOF is controlled by the CO* → CO$_{(g)}$ step due to their strong CO* binding (solid pathways in Region 3) leading to a positive ΔG of CO desorption. Indeed, experimentally, the CO TOF values of the Mn, Co, and Fe–N–C level off or slow down, while the hydrogen evolution accelerates.

We note that the relatively strong binding of CO* on Fe–N$_x$ and Mn–N$_x$ single sites predicted for Region 3 is fully supported by the experimentally confirmed exclusive ability of these two catalysts to produce the hydrocarbon CH$_4$, see Fig. 4. In simple terms, one could say that to produce subsequent reaction products from CO during the CO$_2$RR, the CO molecule must be bound strong and long enough to undergo subsequent dissociation and hydrogenation steps to arrive at CH$_4$. For the Ni and Cu catalysts, the CO* detaching is energetically all downhill reaction which prevents further transformations. This makes Ni–N$_x$ and Cu–N$_x$ single-site catalysts ideal electrochemical CO producers. We note that the experimentally observed reactivity trend of the Cu–N$_x$ catalysts in region 3 does not closely follow that of Ni. This is due to a DFT-predicted thermodynamic instability (not shown) of the Cu–N$_x$ moiety under the strongly reducing conditions of $< -0.7 V_{RHE}$ in region 3. As a result of this, the N-coordinated Cu ions spontaneously reduce to metallic Cu nanoparticles—as confirmed by our XPS results—which show lower CO efficiency and lower TOF values at electrode potentials of region 3[3, 23].

Discussion

In this work, we found a family of solid, single site, N-coordinated transition metal-functionalized nanoporous carbons that show very high electrocatalytic reactivity and selectivity with respect to the direct CO$_2$ reduction to CO (CO$_2$RR). A technical challenge in these M—N—C catalyst is to achieve a high density of active M–N$_x$ sites, while minimizing effects of other nitrogen moieties and inorganic metal impurities, which, for this class of materials cannot be completely excluded. However, based on our experimental observation, we could confirm that the M–N$_x$ site play the dominant role during the CO$_2$RR process into CO. For instance, the Co–N$_x$ sites were efficient hydrogen producers whereas the Fe- and Ni–N$_x$ single site catalysts showed a unique reactivity and faradaic efficiency for reducing CO$_2$ into CO, meeting and exceeding the mass-based activity of state-of-art Au catalysts at a fraction of their cost.

To understand the trends in reactivity and selectivity of the single site catalysts we have correlated our experimental results with DFT simulations of the energetics of the competing reaction pathways involved. Our results demonstrate that the binding energies can be used as descriptors to predict the CO$_2$RR activity and selectivity of this class of catalysts. This is why we find a good agreement between the DFT predictions and the catalytic experiments offering a detailed mechanistic understanding of the role of the metal centers in the considered catalytic processes.

Consistent with experiments, Co–N$_x$ sites displayed all-downhill energetics for hydrogen, but severe energetic barriers to CO formation. By contrast, the low H* and CO* binding energy of the Ni–N$_x$ single site required larger overpotentials to jump start the reactions. At larger overpotentials, however, Ni–N$_x$ catalysts displayed all-downhill energetics toward CO, while hydrogen evolution is hindered.

The high CO efficiency at medium and large overpotentials of the Fe–N–C and Ni–N–C materials combined with their earth-abundant constituents, compared with standard Au catalysts, makes them attractive catalysts for deployment in future industrial CO$_2$-consuming CO cathodes for use as counter electrode process in the chlorine production industry. The choice of catalyst thereby becomes a tradeoff between voltage efficiency (Fe produces most CO at lower potentials) and turnover frequency/current density (Ni makes most CO at higher overpotentials). In particular for Ni–N–C catalysts, high CO efficiencies at current densities approaching industrial levels make them suitable candidates for CO$_2$-consuming gas-diffusion cathode (CCC) designs to be deployed in next-generation chloralkaline electrolyzers. By eliminating the need for fossil fuel-based steam reforming toward purified CO feed streams in the Chlorine-mediated polymer industry, CO$_2$ reuse in chlorine–CO co-electrolyzers would significantly contribute to a lowering of industrial CO$_2$ emissions worldwide.

Methods

Synthesis. All chemicals were used as received. Typically, 4,4′-Dipyridyl hydrate (bipy, 1.114 g, Sigma-Aldrich Co.) was dissolved in 100 mL ethanol solution. A certain amount of CoCl$_2$·6H$_2$O (1.2 g) was dissolved in 900 mL DI water solution. Then the bipy solution was mixed with a CoCl$_2$·6H$_2$O solution and left standing for 24 h without stirring. Then, 50 mL CuCl$_2$·2H$_2$O (0.1 M) solution was rapidly mixed with the bpy-Co^{2+} solution and aged for 4 h. Subsequently, the resultant product was collected by centrifugation with the speed of 4200 r.p.m. for 12 min. After drying, the polymer product was carbonized at 500 °C for 2 h at a heating rate of 60 °C h^{-1} in Ar atmosphere. Finally, hydrophilic N-doped porous carbons (N–C) with trace amounts of Cu were obtained after leaching in 4 M HNO$_3$ for 24 h.

Subsequently, additional transition metal species (M=Mn, Fe, Co, Ni) were introduced in N–C through incipient impregnation of MCl$_x$ solutions. The nominal weight concentration of M respective to N–C was set to 25 wt%. The dried M–N–C composite was re-pyrolyzed at 900 °C for 2 h at a heating rate of 2.0 °C min^{-1} in Ar atmosphere. The carbonized M–N–C was dispersed in aqueous sulfuric acid (ca. 2.0 mol L^{-1}) and refluxed at 100 °C for 1 day. The leached sample was collected and washed with DI water until pH value close to neutral. Finally, the leached sample was treated at 900 °C first in Ar for 2 h, and then in H$_2$ for another 1 h, then again in Ar, let cool down and harvest the final M–N–C electrocatalysis (M=Mn, Fe, Co, Ni). The Cu–N–C material was obtained directly after the reductive annealing procedure without any additional acid leaching.

Physico-chemical characterization. Scanning electron microscope (SEM) investigations were carried out with a Hitachi SU8020 instrument. A FEI Tecnai G2 F20 microscope that was equipped with HAADF-STEM and EDAX detectors was employed to acquire the HAADF-STEM images and EDX elemental maps. XPS measurements were carried out in an ultra-high vacuum (UHV) system equipped with a monochromatic Al Kα X-ray source (1486.6 eV; anode operating at 12.25 kV and 300 W) and a high-resolution Phoibos 150 MCD analyzer (SPECS). X-ray photoemission spectra were measured in fixed analyzer transmission mode with a pass energy of 15 eV and step size of 0.5 and 0.05 eV for survey and high-resolution region scans correspondingly. The binding energy scale was adjusted assigning the signal of graphitic carbon to 285 eV. Raman spectra were measured on a Renishaw Ramascope RM 2000 Raman microscope (×50, na = 0.75) with a REM Laser from Laserquantum (wavelength: 532 nm). The peak parameters were extracted by curve fitting on the Renishaw Wire 2.0 software, where a mixed Gaussian and Lorentzian function was used, and the maximum of the first curve is defined on 1170 cm^{-1}. Nitrogen sorption isotherms were measured on a BELSORP adsorption analyzer at liquid nitrogen temperature. The specific surface area was calculated based on adsorption points in the relative pressure of 0.05 < P/P0 < 0.20 according to Brunauer–Emmett–Teller (BET) theory. Pore size distributions (PSDs) were derived from the adsorption branches of the isotherms based on Non Localized Density Functional Theory (NLDFT, nitrogen on carbon slit adsorption branch kernel). Water physisorption measurements were carried out on a Quantachrome Hydrosorb 1000. CO$_2$ adsorption isotherms were measured on a Autosorb iQ MP micropore analyzers at 273 K. Before gas or vapor physisorption measurements, the samples were degassed at 150 °C for at least 12 h.

Electrochemical measurements. The electrochemical measurements were controlled with EC-Lab SP-200 Potentiostat. Resistance between reference electrode and working electrode was measured with Potential Electrochemical Impedance Spectroscopy (PEIS). 50% of the resistance was corrected by the software and the rest was manually corrected. CO$_2$ electrolysis was carried out in a custom-made two-compartment cell, in which the working electrode was separated from the

counter electrode by Nafion membrane to hinder the re-oxidation of the products on the counter electrode. The glassware was cleaned in nochromix mixed sulfuric acid bath and afterwards in concentrated HNO_3 for 1 h, respectively, rinsed and sonicated with 80 °C ultrapure water several times, and dried at 60 °C in an oven. Each compartment of the cell was filled with 40 mL CO_2 (Air liquid 4.5, flow from button, rate: 30 mL min^{-1}) purged electrolyte. A Pt mesh 100 (Sigma-Aldrich 99.9%) was used as counter electrode (CE) and a leak-free Ag/AgCl electrode (Hugo Sachs Elektronik Harvard apparatus GmbH) was used as the reference electrode. The CO_2 free measurements were carried out in N_2-saturated 0.1 M KH_2PO_4/K_2HPO_4 (Sigma-Aldrich, pH of 6.9), while the CO_2 electrolysis in presence of CO_2 was done in 0.1 M $KHCO_3$ (Sigma-Aldrich, pH of 6.8).

Catalytic product analysis. After 15 min and 60 min of bulk CO_2 electrolysis at constant working potential, a sample of the gas was analyzed by gas chromatography (Shimadzu GC 2014, Haye.Sep Q (Col-No. CS 1015-03) + Haye.Sep R (Col-No. CS 1015-07), TCD and FID detector) to quantify the instant Production Rate and Faradaic Selectivity of the gaseous products. In addition, 2 ml of the electrolyte after reaction was analyzed by high performance liquid chromatograph (HPLC Agilent 1200, Zimmer Chromatography® Column, RID detector) to measure formic acid concentration and analyzed by liquid injection gas chromatography (Shimadzu GC 2010 plus, Fused-Silica-Capillary Column, REF 72306030, FID Detector) for alcohol products.

DFT calculations and predictions. The porphyrin-like structure was created in ASE[57] by a 3×5 unit cell of graphene and functionalized by removing carbon atoms to create the metal-nitrogen site. Further, the outmost carbon atoms were fixed in position and periodic boundaries were applied. This setup is hereby almost similar to Tripcovic[47] and revealed similar results when applying the same references. For the electronic calculations the projector augmented wave method together with spin polarization and the revised Perdew–Burke–Ernzerhof (RPBE)[58] functional was performed with the GPAW software[59, 60]. We applied a 0.18 grid spacing together with a $(2 \times 2 \times 1)$ k-point sampling and all the structure were relaxed to a force below 0.1 eV/Å. To calculate the free energy diagrams, the hydrogen electrode was employed[61]. For this we use zero point, entropy and heat capacity values from reference[62]. Finally, the CO_2 calculated RPBE energy was corrected by 0.45 eV together with a –COH water correction of 0.25 eV and a *CO water correction of 0.1 eV[63].

References

1. Huei-Ru, M. J., Sichao, Ma. & Paul, J. A. K. Electrochemical conversion of CO_2 to useful chemicals: current status, remaining challenges, and future opportunities. *Curr. Opin. Chem. Eng.* **2**, 191–199 (2013).
2. Jacob, S., Jia, H., Muckerman, J. T. & Fujita, E. Thermodynamics and kinetics of CO_2, CO, and H+binding to the metal centre of CO_2 reductioncatalysts. *Chem. Soc. Rev.* **41**, 2036–2051 (2012).
3. Hori, Y., Murata, A. & Takahashi, R. Formation of hydrocarbons in the electrochemical reduction of carbon dioxide at a copper electrode in aqueous solution. *J. Chem. Soc. Faraday Trans.* **85**, 2309–2326 (1989).
4. Akira, M. & Hori, Y. Product selectivity affected by cationic species in electrochemical reduction of CO_2 and CO at a Cu electrode. *Bull. Chem. Soc. Jpn* **64**, 123–127 (1991).
5. Varela, A. S., Kroschel, M., Reier, T., Strasser, P. Controlling the selectivity of CO_2 electroreduction on copper: the effect of the electrolyte concentration and the importance of the local pH. *Catal. Today* **260**, 8–13 (2015).
6. Varela, A. S., Ju, W., Reier, T. & Strasser, P. Tuning the catalytic activity and selectivity of Cu for CO_2 electroreduction in the presence of halides. *ACS Catal.* **6**, 2136–2144 (2016).
7. Kuhl, K., Cave, E., Abram, D. N. & Jaramillo, T. F. New insights into the electrochemical reduction of carbon dioxide on metallic copper surfaces. *Energy Environ. Sci.* **5**, 7050–7059 (2012).
8. Tang, W. et al. The importance of surface morphology in controlling the selectivity of polycrystalline copper for CO_2 electroreduction. *Phys. Chem. Chem. Phys.* **14**, 76–81 (2012).
9. Li, C. W. & Kanan, M. W. CO_2 reduction at low overpotential on Cu electrodes resulting from the reduction of thick Cu_2O Films. *J. Am. Chem. Soc.* **134**, 7231–7234 (2012).
10. Mistry, H. et al. Highly selective plasma-activated copper catalysts for carbon dioxide reduction to ethylene. *Nat. Commun* **7**, 12123 (2016).
11. Schouten, K. J. P., Q., Z., Gallent, E. P. & Koper, M. T. M. Two pathways for the formation of ethylene in CO reduction on single-crystal copper electrodes. *J. Am. Chem. Soc.* **134**, 9864–9867 (2012).
12. Calle-Vallejo, F. & Koper, M. T. M. Theoretical considerations on the electroreduction of CO to C2 species on Cu(100) electrodes. *Angew. Chem. Int. Ed.* **125**, 7423–7426 (2013).
13. Hori, Y., Takahashi, I., Koga, O. & Hoshi, N. Electrochemical reduction of carbon dioxide at various series of copper single crystal electrodes. *J. Mol. Catal. A Chem.* **199**, 39–47 (2003).
14. Roberts, F. S., Kuhl, K. P. & Nilsson, A. A. High selectivity for ethylene from carbon dioxide reduction over copper nanocube electrocatalysts. *Angew. Chem. Int. Ed.* **127**, 5268–5271 (2015).
15. Reske, R., Mistry, H., Behafarid, F., Roldan Cuenya, B. & Strasser, P. Particle size effects in the catalytic electroreduction of CO_2 on Cu nanoparticles. *J. Am. Chem. Soc.* **136**, 6978–6986 (2014).
16. Mistry, H. et al. Tuning catalytic selectivity at the mesoscale via interparticle interactions. *ACS Catal.* **6**, 1075–1080 (2016).
17. Mistry, H., Varela, A. S., Kühl, S., Strasser, P. & Cuenya, B. R. Nanostructured electrocatalysts with tunable activity and selectivity. *Nat. Rev. Mater.* **1**, 16009 (2016).
18. Zhang, S. et al. Polymer-supported CuPd nanoalloy as a synergistic catalyst for electrocatalytic reduction of carbon dioxide to methane. *Proc. Natl Acad. Sci.* **112**, 15809–15814 (2015).
19. Rasul, S. et al. A highly selective copper–indium bimetallic electrocatalyst for the electrochemical reduction of aqueous CO_2 to CO. *Angew. Chem. Int. Ed.* **127**, 2174–2178 (2015).
20. Sarfraz, S., Garcia-Esparza, A. T., Jedidi, A., Cavallo, L. & Takanabe, K. Cu–Sn bimetallic catalyst for selective aqueous electroreduction of CO_2 to CO. *ACS Catal.* **6**, 2842–2851 (2016).
21. Lu, Q., Rosen, J. & Jiao, F. Nanostructured metallic electrocatalysts for carbon dioxide reduction. *ChemCatChem* **7**, 1–11 (2015).
22. Mistry, H. et. al. Enhanced carbon dioxide electroreduction to carbon monoxide over defect-rich plasma-activated silver catalysts. *Angew. Chem. Int. Ed.* **56**, 11394–11398 (2017).
23. Hori, Y. in *Modern Aspects of Electrochemistry* Vol. 42 (ed. Vayenas, C.) Ch. 3, 89–189 (Springer, 2008).
24. Chen, Y., Li, C. W. & Kanan, M. W. Aqueous CO_2 reduction at very low overpotential on oxide-derived Au nanoparticles. *J. Am. Chem. Soc* **134**, 19969–19972 (2012).
25. Zhu, W. et al. Monodisperse Au nanoparticles for selective electrocatalytic reduction of CO_2 to CO. *J. Am. Chem. Soc* **135**, 16833–16836 (2013).
26. Zhu, W. et al. Active and selective conversion of CO_2 to CO on ultrathin Au nanowires. *J. Am. Chem. Soc* **136**, 16132–16135 (2014).
27. Mistry, H. et al. Exceptional size-dependent activity enhancement in the electroreduction of CO_2 over Au nanoparticles. *J. Am. Chem. Soc.* **136**, 16473–16476 (2014).
28. Jovanov, Z. P. et al. Opportunities and challenges in the electrocatalysis of CO_2 and CO reduction using bifunctional surfaces: a theoretical and experimental study of Au–Cd alloys. *J. Catal.* **343**, 215–231 (2016).
29. Hammouche, M., Lexa, D. & Savéant, J. M. Catalysis of the electrochemical reduction of carbon dioxide by iron("0") porphyrins. *J. Electroanal. Chem. Interfacial Electrochem.* **249**, 347–351 (1988).
30. Bhugun, I., Lexa, D. & Savéant, J.-M. Catalysis of the electrochemical reduction of carbon dioxide by iron (0) porphyrins: synergistic effect of weak Brönsted acids. *J. Am. Chem. Soc.* **118**, 1769–1776 (1996).
31. Costentin, C., Drouet, S., Robert, M. & Savéant, J.-M. A local proton source enhances CO_2 electroreduction to CO by a molecular Fe catalyst. *Science* **338**, 90–94 (2012).
32. Kornienko, N. et al. Metal–organic frameworks for electrocatalytic reduction of carbon dioxide. *J. Am. Chem. Soc.* **137**, 14129–14135 (2015).
33. Varela, A. S. et al. Metal-doped nitrogenated carbon as an efficient catalyst for direct CO_2 electroreduction to CO and hydrocarbons. *Angew. Chem. Int. Ed.* **54**, 10758–10762 (2015).
34. J. Shen, M. J. Kolb, A. J. Göttle, M. T. M. Koper DFT study on the mechanism of the electrochemical reduction of CO_2 catalyzed by cobalt porphyrins. *J. Phys. Chem. C* **120**, 15714–15721 (2016).
35. Shen, J. et al. Electrocatalytic reduction of carbon dioxide to carbon monoxide and methane at an immobilized cobalt protoporphyrin. *Nat. Commun.* **6**, 8177 (2015).
36. Wu, G., More, K. L., Johnston, C. M. & Zelenay, P. High-performance electrocatalysts for oxygen reduction derived from polyaniline, iron, and cobalt. *Science* **332**, 443–447 (2010).
37. Sahraie, N. R., Paraknowitsch, J. P., Göbel, C., Thomas, A. & Strasser, P. Noble-metal-free electrocatalysts with enhanced ORR performance by task-specific functionalization of carbon using ionic liquid precursor systems. *J. Am. Chem. Soc.* **136**, 14486–14497 (2014).

38. Sahraie, N. R. et al. Quantifying the density and utilization of active sites in non-precious metal oxygen electroreduction catalysts. *Nat. Commun.* **6**, 8618 (2015).

39. Masa, J., Xia, W., Muhler, M. & Schuhmann, W. On the role of metals in nitrogen-doped carbon electrocatalysts for oxygen reduction. *Angew. Chem. Int. Ed.* **54**, 2–21 (2015).

40. Kramm, U. I. et al. Structure of the catalytic sites in Fe/N/C-catalysts for O_2-reduction in PEM fuel cells. *Phys. Chem. Chem. Phys.* **14**, 11673–11688 (2012).

41. Kumar, B. et al. Renewable and metal-free carbon nanofibre catalysts for carbon dioxide reduction. *Nat. Commun.* **4**, 2819 (2013).

42. Zhang, S. et al. Polyethylenimine-enhanced electrocatalytic reduction of CO_2 to formate at nitrogen-doped carbon nanomaterials. *J. Am. Chem. Soc.* **136**, 7845–7848 (2014).

43. Sharma, P. P. et al. Nitrogen-doped carbon nanotube arrays for high-efficiency electrochemical reduction of CO_2: on the understanding of defects, defect density, and selectivity. *Angew. Chem. Int. Ed.* **54**, 13701–13705 (2015).

44. Jingjie, W. et al. Incorporation of nitrogen defects for efficient reduction of CO_2 via two-electron pathway on three-dimensional graphene foam. *Nano Letter* **16**, 466–470 (2016).

45. Xu, J. et al. Revealing the origin of activity in nitrogen-doped nanocarbons towards electrocatalytic reduction of carbon dioxide. *Chemsuschem* **9**, 1085–1089 (2016).

46. Jingjie, W. et al. A metal-free electrocatalyst for carbon dioxide reduction to multi-carbon hydrocarbons and oxygenates. *Nat. Commun.* **7**, 13869 (2016).

47. Tripkovic, V. et al. Electrochemical CO_2 and CO reduction on metal-functionalized porphyrin-like graphene. *J. Phys. Chem. C* **117**, 9187–9195 (2013).

48. Bagger, A., Ju, W., Varela, A. S., Strasser, P. & Rossmeisl, J. Single site porphyrine-like structures advantages over metals for selective electrochemical CO_2 reduction. *Catal. Today* **288**, 74–78 (2017).

49. Hao, G.-P. et al. Structurally designed synthesis of mechanically stable poly (benzoxazine-co-resol)-based porous carbon monoliths and their application as high-performance CO_2 capture sorbents. *J. Am. Chem. Soc.* **133**, 11378–11388 (2011).

50. Kabir, S., Artyushkova, K., Kiefer, B. & Atanassov, P. Computational and experimental evidence for a new TM–N 3/C moiety family in non-PGM electrocatalysts. *Phys. Chem. Chem. Phys.* **17**, 17785–17789 (2015).

51. Artyushkova, K. et al. Density functional theory calculations of XPS binding energy shift for nitrogen-containing graphene-like structures. *Chem. Commun.* **49**, 2539–2541 (2013).

52. C. D. Wagner et al. NIST Standard Reference Database 20. (2003).

53. Li, Y., Su, H., Chan, S. H. & Sun, Q. CO_2 electroreduction performance of transition metal dimers supported on graphene: a theoretical study. *ACS Catal.* **5**, 6658–6664 (2015).

54. Back, S., Lim, J., Kim, N.-Y., Kim, Y.-H. & Jung, Y. Single-atom catalysts for CO_2 electroreduction with significant activity and selectivity improvements. *Chem. Sci.* **8**, 1090–1096 (2017).

55. Shen, H., Li, Y. & Sun, Q. CO_2 electroreduction performance of phthalocyanine sheet with mn dimer: a theoretical study. *J. Phys. Chem. C* **121**, 3963–3969 (2017).

56. M. Busch et al. Beyond the top of the volcano? – A unified approach to electrocatalytic oxygen reduction and oxygen evolution. *Nano Energy* **29**, 2211–2855 (2016).

57. Bahn, S. R. & Jacobsen, K. W. An object-oriented scripting interface to a legacy electronic structure code. *Comput. Sci. Eng.* **4**, 56–66 (2002).

58. Hammer, B. H., Hansen, L. B. & Nørskov, J. K. Improved adsorption energetics within density-functional theory using revised perdew-burke-ernzerhof functionals. *Phys. Rev. B* **59**, 7413–7421 (1999).

59. Mortensen, J. J., Hansen, L. B. & Jacobsen, K. W. Real-space grid implementation of the projector augmented wave method. *Phys. Rev. B* **71**, 035019 (2005).

60. Enkovaara, J. R. et al. Electronic structure calculations with GPAW: a real-space implementation of the projector augmented-wave method. *J. Phys.: Condens. Matter* **22**, 253202 (2010).

61. Nørskov, J. K. et al. Origin of the overpotential for oxygen reduction at a fuel-cell cathode. *J. Phys. Chem. B* **108**, 17886–17892 (2004).

62. Chan, K., Tsai, C., Hansen, H. A. & Nørskov, J. K. Molybdenum sulfides and selenides as possible electrocatalysts for CO_2 reduction. *ChemCatChem* **6**, 1899–1905 (2014).

63. Peterson, A. A., Abild-Pedersen, F., Studt, F., Rossmeisl, J. & Nørskov, J. K. . How copper catalyzes the electroreduction of carbon dioxide into hydrocarbon fuels. *Energy Environ. Sci.* **3**, 1311–1315 (2010).

Author contributions

P.S., W.J., and A.S.V. conceived and designed the experiments. J.R. and A.B. performed the DFT calculation. S.K., B.R.C., G.-P.H., I.S., and B.V. carried out the chemical synthesis, microscopic and spectroscopic characterization of the carbon-based materials and subsequent in depth data analysis. W.J. and A.S.V. carried out the electrocatalytic tests and analyzed the results. G.-P.H., P.S. and W.J. aggregated the figures and co-wrote the manuscript. All authors discussed the results, drew conclusions, and commented on the manuscript.

Additional information

Supplementary Information accompanies this paper at doi:10.1038/s41467-017-01035-z.

Competing interests: The authors declare no competing financial interests.

Reprints and permission information is available online at http://npg.nature.com/reprintsandpermissions/

Publisher's note: Springer Nature remains neutral with regard to jurisdictional claims in published maps and institutional affiliations.